

A Purely Data-Driven Adaptive Impedance Matching Method Robust to Parasitic Effects

Wendong Cheng, Li Chen, *Senior Member, IEEE* and Weidong Wang

Abstract—Adaptive impedance matching between antennas and radio frequency front-end (RFFE) power modules is essential for mobile communication systems. To address the matching performance degradation caused by parasitic effects in practical tunable matching networks (TMN), this paper proposes a purely data-driven adaptive impedance matching method that avoids trial-and-error physical adjustment. First, we propose the residual enhanced circuit behavior modeling network (RECBM-Net), a deep learning model that maps TMN operating states to their scattering parameters (S-parameters). Then, we formulate the matching process based on the trained surrogate model as a mathematical optimization problem. We employ two classic numerical methods with different online computational overhead, namely simulated annealing particle swarm optimization (SAPSO) and adaptive moment estimation with automatic differentiation (AD-Adam), to search for the matching solution. To further reduce the online inference overhead caused by repeated forward propagation through RECBM-Net, we train an inverse mapping solver network (IMS-Net) to directly predict the optimal solution. Simulation results show that RECBM-Net achieves exceptionally high modeling accuracy. While AD-Adam significantly reduces computational overhead compared to SAPSO, it sacrifices slight accuracy. IMS-Net offers the lowest online overhead while maintaining excellent matching accuracy.

Index Terms—Adaptive impedance matching, tunable matching network, parasitic effects, deep neural network.

I. INTRODUCTION

THE impedance mismatch between the antenna and the radio frequency (RF) front-end power module reduces the power transmitted to the antenna and degrades overall system performance in mobile communication systems. Furthermore, impedance mismatch adversely affects the linearity of the digital pre-distortion power amplifier [1], resulting in signal modulation distortion and spectrum expansion. More critically, the reflected power caused by the mismatch may damage the RF front-end (RFFE) components [2]. Therefore, achieving impedance matching is crucial for mobile devices to maintain reliable and high-performance communication.

The antenna impedance of mobile devices is influenced by multiple factors, e.g. operating frequency [3], various electromagnetic interactions arising from user holding methods [4], [5], user proximity [6], [7], and even user age and clothing [8], etc. The dynamic operating conditions of these devices induce impedance mismatches in the time-frequency domain. To mitigate the detrimental effects of impedance mismatch,

extensive research has been conducted on adaptive impedance matching techniques for mobile communication systems.

Traditional adaptive impedance matching is primarily achieved through numerical methods. The numerical methods use the feedback signal reflecting the degree of mismatch to determine the optimal matching solution through extensive trial and error. The works in [9]–[11] adopted sequential search strategies based on matching performance feedback. To enhance search efficiency, the authors in [12] employed various gradient-free optimization methods to minimize the magnitude of the reflection coefficient, such as the single-step and powell algorithms. Additionally, the work in [13]–[15] employed heuristic algorithms, while the work in [16] utilized gradient information to perform steepest gradient descent, reducing the number of trial-and-error iterations. The authors in [17] observed that when the parallel inductance of the T-network is fixed, the real part of the input impedance follows a linear fractional relationship with the reactance of the first series element, and proposed a binary search algorithm to reduce the number of iterations. The disadvantages of numerical methods are their inefficiency and riskiness. As the matching network components must be physically adjusted during each trial, this tuning process introduces both amplitude and phase modulation to the radiated signal, which can lead to data corruption if tuning occurs during transmission [18]. Therefore, numerical methods prove impractical for achieving adaptive impedance matching in mobile devices.

Compared to numerical methods, analytical methods derive the matching solution directly from accurate complex impedance information and the circuit model, thereby avoiding the iterative trial and error procedures. The authors in [19] proposed a method for real-time measurement of the complex impedance at any location within the RFFE of a handset based on perturbation theory, providing critical support for the analytical computation of the matching solution. The work of [20] presented explicit mathematical expressions for the values of components when the ideal π -network is perfectly matched. Furthermore, the authors in [21] developed an orthogonal detection technique that directly sets the real and imaginary parts of the impedance. To address imperfect matching caused by the limited tuning range of practical π -network, the work of [22] proposed an analytical method to compute the optimal solution within the tunable range. Additionally, the work of [23] considered the parasitic effects introduced by MEMS components in the practical π -network and provided an analytical solution by solving the conjugate matching equation of the equivalent circuit, which remains an approximation of the practical circuit. As analytical methods are inherently model-

Wendong Cheng, Li Chen and Weidong Wang are with the CAS Key Laboratory of Wireless Optical Communication, University of Science and Technology of China (USTC), Hefei 230027, China (e-mail: cwd01@mail.ustc.edu.cn; chenli87@ustc.edu.cn; wdwang@ustc.edu.cn).

dependent, the accuracy of the matching is determined by the degree of conformity between the practical circuit model and the model assumed by the algorithm.

Recently, powerful artificial intelligence (AI) technologies have been applied to achieve efficient and accurate adaptive impedance matching. To address impedance mismatch in the frequency domain, the work in [24] proposed a deep learning model that maps the desired reflection coefficient frequency response to the corresponding L-network configuration for a given planner inverted-F antenna. Considering the complexity of the model, the authors in [25] proposed a low-complexity shallow learning model based on ridge regression to achieve the same mapping. In addition, to address the impedance mismatch caused by variations in the distance between the transmitting and receiving coils in wireless power transfer systems, the work in [26] employed a neural network to establish a mapping between the equivalent load impedance and the corresponding matching solution at a specific frequency. Furthermore, considering time-frequency domain mismatch, the work of [27] proposed a deep neural network (DNN) to directly determine the ideal π -network matching solution based on incomplete impedance information. The construction of large and accurate supervised datasets is critical to the success of AI-based adaptive impedance matching methods.

The above analytical and AI-based methods are applicable only to tunable matching networks (TMN) that either neglect parasitic effects or consider only simplified cases. However, parasitic effects in practical tunable matching networks (TMN) are unavoidable and complex due to inherent limitations in the process of manufacturing and packaging of RF circuits. For example, common structures such as traces, bonding wires [28], vias [29], pins [30], solder balls [31], etc., will introduce parasitic capacitance, inductance, and resistance. Particularly in mobile communication systems, TMNs are often implemented using discrete electronically switchable inductor and capacitor banks [32] to satisfy miniaturization constraints. The dense integration of switches, transmission lines, and non-ideal discrete components significantly aggravates parasitic effects.

Parasitic effects render the equivalent circuit topology of a practical TMN unknown. When these effects are taken into account, matching solutions derived from analytical methods based on idealized or specific topologies often fail to meet the actual matching requirements. Similarly, for the aforementioned AI-based methods, datasets constructed from idealized topologies fail to reflect real matching behavior, while those based on practical topologies suffer from the difficulty of acquiring accurate labels. These issues lead to degraded matching performance in AI-based methods as well. To the best of our knowledge, achieving efficient and accurate adaptive impedance matching remains an open problem when parasitic effects cause the practical TMN to deviate from its idealized topology.

To address this challenge, in this paper, we propose a purely data-driven adaptive impedance matching method. First, we analyze the impact of parasitic effects on the behavior of TMN using multiport network theory. Considering the high nonlinearity and uncertainty introduced by these parasitic effects, we propose a deep learning model, residual

enhanced circuit behavior modeling network (RECBM-Net), to accurately learn the system behavior. Based on the trained RECBM-Net, we further develop three matching solution determination strategies with varying online computational overhead: simulated annealing particle swarm optimization (SAPSO), adaptive moment estimation with automatic differentiation (AD-Adam), and an inverse mapping solver network (IMS-Net) that directly infers the matching solution. Our main contributions are summarized as follows:

- **Behavioral modeling of parasitic effects in TMNs via multiport network theory and DNN.** First, we analyze the advantages of using scattering parameters (S-parameters) to characterize the circuit behavior of TMNs, and derive a general expression for the S-parameters of an arbitrary two-port TMN. Then, we explain the challenges associated with analytically constructing this general expression, and discuss the feasibility of employing deep learning for behavioral modeling. To characterize the circuit behavior of TMN while explicitly accounting for parasitic effects, we propose RECBM-Net, a DNN that learns the mapping between the TMN operating state and its corresponding S-parameters.
- **Reformulating the data-driven adaptive impedance matching as a mathematical optimization problem.** To address the challenges of formulating and solving conjugate matching equations due to the black-box nature of RECBM-Net in characterizing circuit behavior, we reformulate the adaptive impedance matching as a mathematical optimization problem based on the S-parameters. By varying the input to the RECBM-Net, the physical adjustment of tunable elements can be virtually emulated. The objective is to identify a TMN configuration whose S-parameters closely approximate the target transmission characteristics under the matched condition.
- **Efficient matching solution determination strategies based on the RECBM-Net surrogate model.** While brute-force grid search can identify the matching configuration, it incurs substantial online computational overhead due to repeated RECBM-Net evaluations. To reduce the cost of solving the previously formulated optimization problem, we first propose SAPSO, a hybrid algorithm that integrates global exploration with rapid convergence. In addition, we leverage automatic differentiation and employ the adaptive moment estimation (Adam) to enable efficient gradient-based search for a matching solution, further reducing computational overhead. To completely eliminate the need for repeated RECBM-Net evaluations, we introduce IMS-Net, a neural solver trained to directly predict the optimal matching solution.

The remainder of this paper is organized as follows. Section II introduces the adaptive impedance matching system and formulates the matching problem while accounting for parasitic effects. In Section III, we propose a deep learning model RECBM-Net, designed to fit the circuit behavior of the TMN. Section IV presents three strategies for determining matching solutions based on the surrogate model of a practical TMN, each with varying computational overhead. The matching

performance on a practical L-network is evaluated in Section V. Finally, Section VI concludes the paper.

II. SYSTEM MODEL

In this section, we will begin by introducing the adaptive impedance matching system. Next, we will analyze the matching solution for the ideal L-network. Finally, we will examine in detail the complexities introduced by parasitic effects and formulate an adaptive impedance matching problem considering parasitic effects.

A. Adaptive Impedance Matching System

Consider the adaptive impedance matching system depicted in Fig. 1. It is composed of three main modules: a TMN, an impedance sensor, and a control unit. The TMN is typically composed of tunable capacitors and tunable inductors, with common configurations including L-network and π -network. It provides the desired impedance transformation by adjusting the values of reactive components. The impedance sensor detects impedance variations by analyzing the input and reflected signals extracted via a directional coupler. It can provide the control unit with key parameters such as the reflection coefficient and voltage standing wave ratio (VSWR). The control unit employs an adaptive impedance matching method to formulate a strategy for adjusting the TMN.

The control unit generally formulates the corresponding matching strategy based on two distinct types of measurement data [33]. One is the data that only indicates the degree of impedance mismatch, such as reflected power, VSWR, etc. Based on this type of data, the control unit can only adopt a trial-and-error impedance matching strategy. Impedance matching is achieved as quickly as possible by deciding the TMN configuration that is most worth trying each time. The other is the data that fully characterizes the complex impedance (e.g., reflection coefficient). Based on this type of data, the control unit knows the complex input impedance and can directly compute the matching solution based on the circuit model. In order to avoid the impracticality of frequent TMN adjustments, we focus on the latter scenario, in which the control unit can obtain the complex impedance. Also, we assume that the reflection coefficient is measured accurately.

B. Impedance Matching in Ideal L-network

Among the various TMN configurations, the L-network is particularly appealing for its simplicity and efficiency. In the ideal L-network depicted in Fig. 2, the tunable capacitors C_p and C_s enable the necessary impedance transformation. The input impedance Z_{in} after impedance transformation by the L-network is given by

$$Z_{in} = \frac{1}{jB_p + \frac{1}{Z_L + \frac{1}{jB_s}}}, \quad (1)$$

where $B_p = \omega C_p$ and $B_s = \omega C_s$ are the susceptance of C_p and C_s , respectively, Z_L donates the load impedance and ω represents the angular frequency.

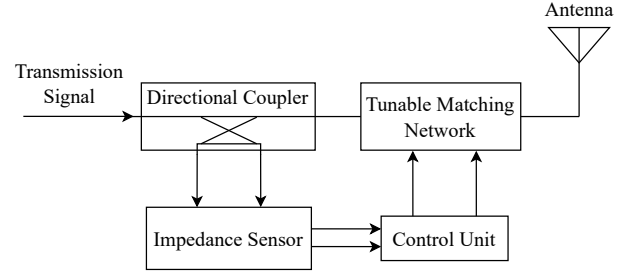


Fig. 1. Block diagram of an adaptive impedance matching system.

Based on Eq. (1), the reflection coefficient characterizes the input impedance can be given by

$$\Gamma_{in} = \frac{Z_{in} - R_S}{Z_{in} + R_S}, \quad (2)$$

where R_S represents the source impedance (typically 50 Ω). Similarly, the load reflection coefficient for the antenna impedance Z_L is defined as

$$\Gamma_L = \frac{Z_L - R_S}{Z_L + R_S}. \quad (3)$$

The maximum power transfer theorem serves as the fundamental principle for tuning TMN to achieve impedance matching for different Γ_L . Maximum power is delivered when the input impedance is the complex conjugate of the source impedance. Since R_S is typically a purely resistive 50 Ω , this condition is reduced to $Z_{in} = R_S$, which in turn implies that the reflection coefficient Γ_{in} measured by the impedance sensor is zero. Accordingly, the values of the C_p and C_s are adjusted to meet this requirement. Donating the load impedance as $Z_L = R_L + jX_L$ and substituting it into Eq. (1), we have the conjugate matching equations as

$$\begin{cases} \frac{B_s^2 R_L}{(B_p B_s R_L)^2 + (B_p + B_s - B_p B_s X_L)^2} = R_S, \\ \frac{2B_p B_s X_L + B_s^2 X_L - B_p B_s^2 (R_L^2 + X_L^2) - B_p - B_s}{(B_p B_s R_L)^2 + (B_p + B_s - B_p B_s X_L)^2} = 0. \end{cases} \quad (4)$$

By solving Eq. (4), we have the closed-form expressions of the capacitor values required for impedance matching as

$$\begin{cases} C_p = \frac{R_L R_S - R_L^2 \pm X_L \sqrt{R_L R_S - R_L^2}}{\omega [R_L X_L R_S \pm R_L R_S \sqrt{R_L R_S - R_L^2}]}, R_S \geq R_L. \\ C_s = \frac{X_L \pm \sqrt{R_L R_S - R_L^2}}{\omega [R_L^2 + X_L^2 - R_L R_S]} \end{cases} \quad (5)$$

C. Impedance Matching with Parasitic Effects

Considering the inherent limitations of the manufacturing process, parasitic parameters may be introduced at any location along the RF channel connecting the antenna to the transmitter's RFFE (e.g., radio frequency integrated circuits or power amplifier modules). As shown in Fig. 2, parasitic effects in RF channel arise from three key aspects.

- **L-network itself parasitics:** These parasitic effects primarily stem from the manufacturing process of the

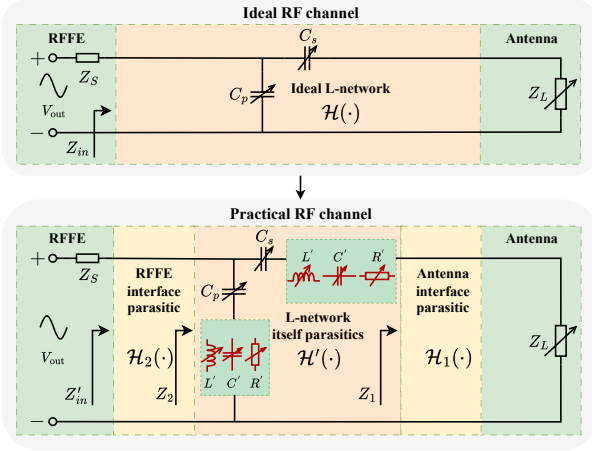


Fig. 2. Comparison between ideal and practical RF channels, illustrating impedance matching using an ideal L-network and the degradation caused by parasitic effects.

TMN itself [34]. Specifically, whether employing continuously tunable components (e.g., varactors [35] or MEMS varactors [36]) or digitally tunable components (e.g., MEMS switches [37], PIN diodes [12], or CMOS switches [38]), each may introduce additional parasitic capacitance, inductance and resistance. In the ideal case, the L-network transforms the load impedance Z_L into the input impedance Z_{in} via the function $\mathcal{H}(\cdot)$, as described by Eq. (1). The presence of parasitic effects modifies this transformation to a new mapping $\mathcal{H}'(\cdot)$, which maps the intermediate impedance Z_1 to $Z_2 = \mathcal{H}'(Z_1; f)$, where f denotes the operating frequency.

- **RFFE interface parasitics:** These parasitic effects arise from the physical interconnection between the TMN and the RFFE. During the PCB routing, via formation and soldering processes [39], connection discontinuities or non-ideal contacts can introduce additional parasitic inductance, capacitance, and resistance. The impedance transformation resulting from these parasitic effects is denoted by $\mathcal{H}_2(\cdot)$, which maps the intermediate impedance Z_2 to the final input impedance $Z'_{in} = \mathcal{H}_2(Z_2; f)$.
- **Antenna interface parasitics:** These parasitic effects arise from the connection process between the TMN and the antenna with mechanisms similar to those discussed for the RFFE interface. The impedance transformation resulting from this portion of the parasitic effects is denoted by $\mathcal{H}_1(\cdot)$, which maps the antenna load impedance Z_L to the intermediate impedance $Z_1 = \mathcal{H}_1(Z_L; f)$.

Above all, due to the presence of parasitic effects, the impedance matching condition for ideal L-network given in Eq. (4) is modified to

$$\mathcal{H}_2(\mathcal{H}'(\mathcal{H}_1(Z_L; f); f); f) = R_S. \quad (6)$$

Neglecting these parasitic effects will lead to impedance matching failure. Taking parasitic effects into account, the overall impedance transformation is expressed as $(\mathcal{H}_2 \circ \mathcal{H}' \circ \mathcal{H}_1)(\cdot)$, which is strongly nonlinear and inherently uncertain. The strong nonlinearity arises from the fact that parasitic

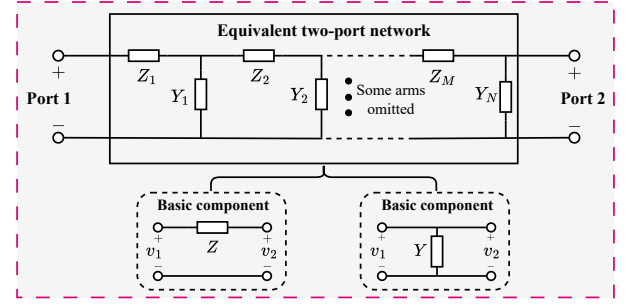


Fig. 3. Equivalent two-port network representation of a practical TMN, where parasitic effects result in a more complex topology consisting of M series arms and N shunt arms.

elements are typically superimposed on RF channel in a mixture of series and shunt configurations. This complex interconnection results in a high-order rational function form for the input impedance. Furthermore, the inherent uncertainty stems from the unpredictable nature of parasitic parameters. Specifically, the types, values and positions of parasitic parameters are unknown, making the exact mathematical form of $\mathcal{H}_1(\cdot)$, $\mathcal{H}_2(\cdot)$ and $\mathcal{H}'(\cdot)$ indeterminate. Consequently, the presence of parasitic effects not only complicates the relationship between the tunable components and the input impedance but also introduces inherent uncertainty, thereby significantly increasing the difficulty of adaptive impedance matching.

In summary, achieving efficient and accurate adaptive impedance matching under parasitic effects requires precise characterization of the modified system behavior $(\mathcal{H}_2 \circ \mathcal{H}' \circ \mathcal{H}_1)(\cdot)$. Based on the analysis above, it is evident that both modeling the circuit behavior of the TMN accurately in the presence of parasitic effects and determining the corresponding matching solution based on the established model remain formidable challenges.

III. BEHAVIORAL MODELING OF CIRCUITS WITH PARASITIC EFFECTS

In this section, we will first employ multiport network theory to demonstrate that S-parameters can effectively characterize the circuit behavior of TMN in the presence of parasitic effects. Subsequently, we will introduce RECBM-Net, a deep learning model designed to fit the TMN behavior.

A. Analyzing TMN Using MultiPort Network Theory

Parasitic effects cause the practical TMN to deviate from the ideal L-network, resulting in a complex and uncertain topology. Therefore, it is not feasible to characterize TMN behavior from the perspective of impedance transformation. By modeling the practical TMN as a two-port network and analyzing it using multiport network theory [40], we can explore the circuit behavior of TMN under parasitic effects without requiring detailed knowledge of internal structure.

Any passive two-port network representing a practical TMN can be equivalently represented as a cascade of series and shunt arms. As illustrated in Fig. 3, the equivalent cascaded network of a practical L-network comprises M series arms and N shunt arms due to the parasitic effects. The transmission

matrix (ABCD-matrix) of a two-port network with a series arm is given by

$$\begin{bmatrix} A_{s,m} & B_{s,m} \\ C_{s,m} & D_{s,m} \end{bmatrix} = \begin{bmatrix} 1 & Z_m \\ 0 & 1 \end{bmatrix}, m = 1, \dots, M, \quad (7)$$

where Z_m represents the impedance of the m -th series arm. Similarly, the ABCD matrix of a two-port network with a shunt arm is given by

$$\begin{bmatrix} A_{p,n} & B_{p,n} \\ C_{p,n} & D_{p,n} \end{bmatrix} = \begin{bmatrix} 1 & 0 \\ Y_n & 1 \end{bmatrix}, n = 1, \dots, N, \quad (8)$$

where Y_n represents the admittance of the n -th shunt arm. By multiplying these matrices in sequence, we obtain the overall ABCD matrix of the two-port network as

$$\begin{bmatrix} A & B \\ C & D \end{bmatrix} = \begin{bmatrix} A_{s,1} & B_{s,1} \\ C_{s,1} & D_{s,1} \end{bmatrix} \begin{bmatrix} A_{p,1} & B_{p,1} \\ C_{p,1} & D_{p,1} \end{bmatrix} \dots \begin{bmatrix} A_{s,M} & B_{s,M} \\ C_{s,M} & D_{s,M} \end{bmatrix} \begin{bmatrix} A_{p,N} & B_{p,N} \\ C_{p,N} & D_{p,N} \end{bmatrix}. \quad (9)$$

If the first arm is shunt (rather than series), the first matrix on the right side of Eq. (9) is set to the identity matrix. Similarly, if the last arm is series (rather than shunt), the last matrix is set to the identity matrix. Consequently, the ABCD matrix of any passive two-port network can be expressed in the general form of Eq. (9), regardless of the specific arrangement of series and shunt arms. Finally, based on the conversion relationship between ABCD matrix and scattering parameters (S-parameters), the S-parameters of the entire two-port network is given by

$$\begin{bmatrix} S_{11} & S_{12} \\ S_{21} & S_{22} \end{bmatrix} = \begin{bmatrix} \frac{A+B/Z_0-CZ_0-D}{A+B/Z_0+CZ_0+D} & \frac{2(AD-BC)}{A+B/Z_0+CZ_0+D} \\ \frac{2}{A+B/Z_0+CZ_0+D} & \frac{-A+B/Z_0-CZ_0+D}{A+B/Z_0+CZ_0+D} \end{bmatrix}, \quad (10)$$

where Z_0 represents the characteristic impedance. The S-parameters describe the reflection and transmission characteristics of n -ports networks in high-frequency. They effectively characterize the circuit behavior of practical TMN in the presence of parasitic effects. In addition, the S-parameters depend exclusively on the network's internal topology and are not influenced by the load impedance.

Equations (9) and (10) establish the S-parameters of a practical TMN as a function of the operating frequency f and the tunable capacitors C_p and C_s . We denote this mapping as

$$\mathbf{S} = \mathcal{F}(f, C_p, C_s), \quad (11)$$

where \mathcal{F} represents the circuit behavior under parasitic effects to be characterized. Based on the preceding network theory analysis, if the detailed topology of the practical TMN is known, a closed-form expression for the mapping \mathcal{F} can be derived. Due to parasitic effects, the exact number of series and shunt arms cannot be determined. Moreover, the specific circuit configurations of these arms are unknown, which prevents the derivation of explicit analytical expressions for Z_m and Y_n . Consequently, an analytical model for the functional relationship \mathcal{F} cannot be established.

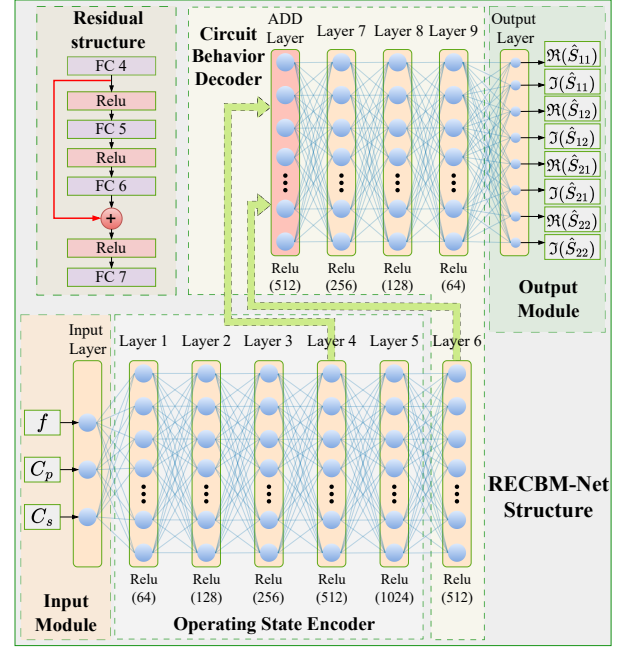


Fig. 4. Architecture of the proposed RECBM-Net. The network comprises five modules: an input module that receives the operating state (f, C_p, C_s), an operating state encoder that extracts high-dimensional features, a residual structure to enhance representation learning, a circuit behavior decoder and an output module that jointly predicts the S-parameters.

B. DNN based modeling

\mathcal{F} is an extremely complex and highly nonlinear function. According to the universal approximation theorem [41], a multi-layer feedforward network with a sufficient number of hidden neurons can approximate any continuous function with arbitrary precision. By training a DNN on the measured S-parameters of the practical TMN, we can obtain an accurate estimate $\hat{\mathcal{F}}$ of the mapping \mathcal{F} . The preceding analysis of the fundamental mathematical representation of \mathcal{F} is crucial, as it confirms the existence of a mathematical relationship between (f, C_p, C_s) and the S-parameters. Leveraging a purely data-driven approach, DNN directly establishes an end-to-end nonlinear mapping. This method fundamentally circumvents the challenge of determining detailed topology while enabling accurate characterization of system behavior under parasitic effects.

The structure of the proposed RECBM-Net is illustrated in Fig. 4. It consists of an input module, a TMN operating state encoder, a circuit behavior decoder, an output module and a residual structure. The input vector is defined as $\mathbf{x} = (f, C_p, C_s) \in \mathbb{R}^3$. The output of the RECBM-Net is an 8-dimensional vector $\mathbf{y} \in \mathbb{R}^8$, where each pair of entries corresponds the real and imaginary components of one of the S-parameters, i.e., $\Re(S_{11})$, $\Im(S_{11})$, $\Re(S_{12})$, $\Im(S_{12})$, $\Re(S_{21})$, $\Im(S_{21})$, $\Re(S_{22})$ and $\Im(S_{22})$. $\Re(\cdot)$ and $\Im(\cdot)$ denote the real and imaginary parts, respectively. The proposed RECBM-Net employs an encoder-decoder structure with nine hidden layers. In operating state encoder module, the hidden layer dimensionality is initially increased to capture deeper and more abstract features from the input. Specifically, the

network progressively expands the feature space with 64, 128, 256, 512, and 1024 neurons. Through the operating state encoder, the 3-dimensional TMN operating state (f, C_p, C_s) is transformed into a 1024-dimensional representation, thereby enabling RECBM-Net to capture the intricate nonlinear relationships between the operating state and the corresponding S-parameters. Subsequently, in the circuit behavior decoder module, the network begins to reduce the dimensionality in the later layers with 512, 256, 128, and 64 neurons, effectively decoding the learned features into a compact representation. The final output layer consists of 8 neurons, directly predicting the real and imaginary parts of the S-parameters.

All layers are fully connected (FC), with rectified linear unit (ReLU) activations applied to the hidden layers to introduce nonlinearity and mitigate the vanishing gradient problem. Additionally, the residual structure is introduced through an add layer after the sixth layer. The output of the fourth layer is directly added to that of the sixth layer, bypassing both the ReLU activations and the intermediate layers between them. Then, the summed output is passed through the ReLU activation function and continues to propagate through the subsequent layers. The residual structure improves gradient flow and alleviates network degradation while enhancing the model's ability for deeper representation learning.

IV. MATCHING SOLUTION DETERMINATION STRATEGY BASED ON SURROGATE MODEL

In this section, we first formulate the task of determining matching solution based on a circuit behavior surrogate model as an mathematical optimization problem. Given the difficulty of solving this problem analytically, we will propose three optimization strategies with varying computational overhead.

A. Formulating the Matching Optimization Problem

The trained RECBM-Net accurately characterizes the behavior of the practical TMN. By employing it as the surrogate model, the matching solution can be computed entirely through simulation, eliminating the need for physical TMN adjustment. An overview of the proposed data-driven adaptive impedance matching process is shown in Fig. 5.

The impedance sensor continuously monitors the input reflection coefficient Γ_{in} . When an impedance mismatch is detected, the load reflection coefficient of the mismatched antenna is initially computed through the RECBM-Net. Based on the current TMN operating state $(f, C_p^{now}, C_s^{now})$, the RECBM-Net predicts the corresponding S-parameters $\hat{\mathbf{S}}_{now}$. Then, the mismatched load reflection coefficient $\hat{\Gamma}_L$ is calculated by

$$\hat{\Gamma}_L = \frac{\Gamma_{in} - \hat{S}_{11}}{\hat{S}_{12} \cdot \hat{S}_{21} + (\Gamma_{in} - \hat{S}_{11}) \cdot \hat{S}_{22}}, \quad (12)$$

where \hat{S}_{11} , \hat{S}_{12} , \hat{S}_{21} and \hat{S}_{22} are the elements of the predicted $\hat{\mathbf{S}}_{now}$. Since the RECBM-Net can predict the S-parameters for any operating state, the input reflection coefficient $\hat{\Gamma}_{in}$ for any configuration can be predicted by

$$\hat{\Gamma}_{in} = \frac{\hat{S}_{12} \cdot \hat{S}_{21} \cdot \hat{\Gamma}_L}{1 - \hat{\Gamma}_L \cdot \hat{S}_{22}} + \hat{S}_{11}, \quad (13)$$

where \hat{S}_{11} , \hat{S}_{12} , \hat{S}_{21} and \hat{S}_{22} are the elements of the predicted S-parameters $\hat{\mathbf{S}}$ for the corresponding operating state. Thus, the matching process reduces to finding the optimal TMN configuration (C_p^*, C_s^*) that minimizes the predicted magnitude of the input reflection coefficient, denoted as $|\hat{\Gamma}_{in}|$.

We denote the mapping from the predicted $\hat{\mathbf{S}}$ and $\hat{\Gamma}_L$ to the magnitude of predicted input reflection coefficient as

$$|\hat{\Gamma}_{in}| = \psi(\hat{\mathbf{S}}, \hat{\Gamma}_L), \quad (14)$$

where $\psi(\cdot)$ denotes taking the magnitude of the reflection coefficient given in Eq. (13). Additionally, the forward propagation of RECBM-Net for predicting $\hat{\mathbf{S}}$ is denoted as $\hat{\mathcal{F}}(f, C_p, C_s)$. Based on this black-box model of TMN behavior, the impedance matching process can be formulated as the following mathematical optimization problem:

$$\begin{aligned} \min_{C_p, C_s} \quad & \psi(\hat{\mathcal{F}}(f, C_p, C_s), \hat{\Gamma}_L) \\ \text{s.t.} \quad & C_{p,\min} \leq C_p \leq C_{p,\max}, \\ & C_{s,\min} \leq C_s \leq C_{s,\max}. \end{aligned} \quad (15)$$

where $C_{p,\min}$ and $C_{p,\max}$ denote the lower and upper limits of C_p , while $C_{s,\min}$ and $C_{s,\max}$ donate those of C_s . In the current mismatch scenario, the operating frequency f and the derived load reflection coefficient $\hat{\Gamma}_L$ are treated as fixed.

B. Strategies for Solving the Matching Problem

Given that the RECBM-Net comprises multiple hidden layers with numerous neurons and activation functions, $\hat{\mathcal{F}}(\cdot)$ is an extremely complex nonlinear function. Embedding $\hat{\mathcal{F}}(\cdot)$ within the objective function $\psi(\cdot)$ further complicates the derivation of an analytical optimal solution. To address this, we first introduce two classic numerical optimization strategies: SAPSO and AD-Adam. These methods require varying numbers evaluations of RECBM-Net to compute the reflection coefficient for each TMN configuration, leading to considerable online computational overhead. To eliminate the need for repeated RECBM-Net inference during optimization, we further propose an inverse mapping solver network (IMS-Net) for RECBM-Net to directly obtain the matching solution.

Classic strategy 1 (SAPSO): SAPSO combines the fast convergence and high accuracy of particle swarm optimization (PSO) with the ability of simulated annealing (SA) to escape local optima by accepting occasionally worse solutions. This hybridization enhances the global search for an optimal TMN configuration. Using SAPSO to obtain the matching solution involves three major steps.

- *Initialization of the population:* Let n indexes particles, and t indexes iterations. At iteration $t = 0$, set each particle's initial position $\mathbf{x}_n^{(0)}$ (representing a candidate TMN configuration) and velocity $\mathbf{v}_n^{(0)}$ within the given constraints. For each particle n , compute the initial fitness $\Gamma_n^{(0)}$ and record both its personal best position $\mathbf{P}_{\text{best},n}^{(0)}$ and the global best position $\mathbf{G}_{\text{best}}^{(0)}$ among all particles. Based on $\mathbf{G}_{\text{best}}^{(0)}$, determine the initial temperature T for the simulated annealing component. Additionally, initialize the compression factor χ and the annealing rate δ .

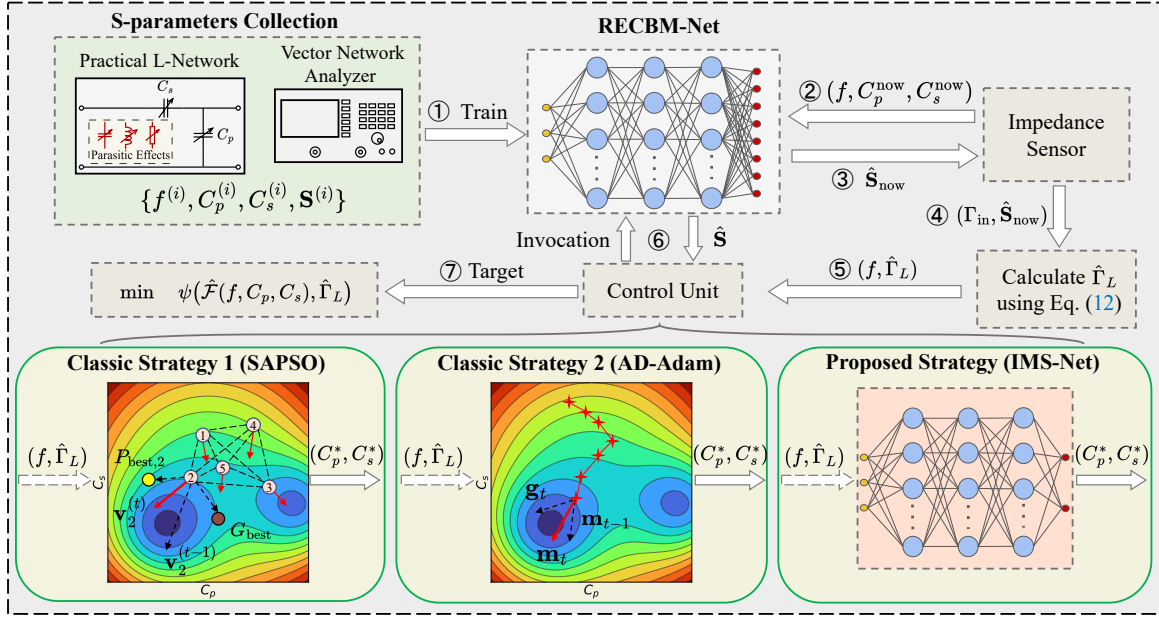


Fig. 5. Overview of the proposed purely data-driven adaptive impedance matching method. The RECBM-Net is first trained using measured S-parameters of the practical L-network. During operation, it predicts the $\hat{\mathbf{S}}_{\text{now}}$ corresponding to the current TMN operating state. According to Eq. (12), the impedance sensor then predicts the $\hat{\Gamma}_L$. Finally, the control unit determines the matching solution based on f and $\hat{\Gamma}_L$. To achieve this, we propose three strategies that differ in the computational overhead.

- **Velocity and position updates:** At iteration t , first calculate the normalized Metropolis acceptance probabilities $p_n^{(t-1)}$ for each particle n based on its personal best fitness $\Gamma_{\text{best},n}^{(t-1)}$. $\Gamma_{\text{best},n}^{(t-1)}$ donates the best fitness value achieved by particle n up to the current iteration. Next, perform a roulette wheel selection using $p_n^{(t-1)}$ to obtain a candidate global best position $\mathbf{G}_{\text{rand}}^{(t-1)}$. Then, update each particle's velocity $\mathbf{v}_n^{(t)}$ and position $\mathbf{x}_n^{(t)}$ by taking into account both $\mathbf{P}_{\text{best},n}^{(t-1)}$ and $\mathbf{G}_{\text{rand}}^{(t-1)}$. If the updated position $\mathbf{x}_n^{(t)}$ violates the predefined bounds of the tunable capacitors, a large penalty value is assigned to its fitness $\Gamma_n^{(t)}$ to discourage infeasible solutions. After this update, refresh the personal best positions $\mathbf{P}_{\text{best},n}^{(t)}$ and their corresponding reflection coefficients $\Gamma_{\text{best},n}^{(t)}$, as well as the global best position $\mathbf{G}_{\text{best}}^{(t)}$ and its corresponding coefficient $\Gamma_{\text{best}}^{(t)}$. Finally, decrease the annealing temperature T .
- **Acceptance criteria and termination:** During each iteration, if the global best fitness Γ_{best} falls below a predefined threshold ε , the algorithm terminates early and outputs the corresponding optimal TMN configuration (C_p^*, C_s^*) . Otherwise, the algorithm continues until the maximum number of iterations \mathcal{I}_{max} is reached and returns the best solution found.

SAPSO is a non-gradient numerical optimization method with the advantage of high accuracy. It updates parameters by evaluating the fitness of all particles in each iteration. Since computing each particle's fitness requires invoking the RECBM-Net to infer the corresponding S-parameters, it is computationally intensive. Algorithm 1 provides the detailed procedure for determine the matching solution based on SAPSO.

Classic strategy 2 (AD-Adam): To reduce the number of RECBM-Net evaluations, we adopt adaptive moment optimization estimation (Adam) algorithm [42], a gradient-based method that efficiently updates parameters using first and second moment estimates of gradients. Adam adaptively adjusts the learning rate of each parameter, thereby achieving faster convergence. The effectiveness of Adam critically depends on accurate gradient computation. Automatic differentiation (AD) [43] enables the exact computation of gradients for complex nonlinear functions by constructing computational graphs and systematically applying the chain rule. It overcomes the limitations of both symbolic and numerical differentiation. Therefore, AD is used to compute the gradient of the objective function $\psi(\hat{\mathcal{F}}(f, C_p, C_s), \hat{\Gamma}_L)$, which becomes highly nonlinear due to the embedding of the RECBM-Net. The main steps to determine the optimal matching solution using the AD-Adam are as follows.

- **Initialization:** Set the learning rate α and exponential decay rates β_1, β_2 . Initialize the matching solution as $\theta_0 = (C_p^{(0)}, C_s^{(0)})$. Additionally, initialize the first-order moment estimate \mathbf{m}_0 (momentum term) and the second-order moment estimate \mathbf{v}_0 for the initial gradient \mathbf{g}_0 .
- **Gradient-based parameter update:** In each iteration t , compute the gradient \mathbf{g}_t of the objective function with respect to $\theta^{(t-1)}$ using AD. Then, update the first-order moment estimate \mathbf{m}_t and second-order moment estimate \mathbf{v}_t based on \mathbf{g}_t , where \odot denotes the Hadamard product. Compute the bias-corrected first-order moment estimate $\hat{\mathbf{m}}_t$ and the bias-corrected second-order moment estimate $\hat{\mathbf{v}}_t$. Next, update the matching solution $\theta^{(t)}$ based on $\hat{\mathbf{m}}_t$ and $\hat{\mathbf{v}}_t$. After the update, $\theta^{(t)}$ is projected onto the feasible set \mathcal{C} to ensure that each parameter remains

Algorithm 1: SAPSO Impedance Matching

Input: Number of particles N , individual learning factor κ_1 , social learning factor κ_2 , cooling factor λ , maximum iterations \mathcal{I}_{\max} , load reflection $\hat{\Gamma}_L$, frequency f , threshold ε , tuning range $\mathcal{C} = [C_{p,\min}, C_{p,\max}] \times [C_{s,\min}, C_{s,\max}]$.

Output: Optimal matching solution $\mathbf{C}^* = (C_p^*, C_s^*)$.

- 1 **Initialization:** $\forall n \in \{1, \dots, N\} : \mathbf{x}_n^{(0)} = (x_{n,1}^{(0)}, x_{n,2}^{(0)})$,
 $\mathbf{v}_n^{(0)} = (v_{n,1}^{(0)}, v_{n,2}^{(0)})$, $\Gamma_n^{(0)} = \psi(\hat{\mathcal{F}}(f, \mathbf{x}_n^{(0)}), \hat{\Gamma}_L)$,
 $\mathbf{P}_{\text{best},n}^{(0)} = \mathbf{x}_n^{(0)}$, $\Gamma_{\text{best},n}^{(0)} = \Gamma_n^{(0)}$, $k = \arg \min_n (\Gamma_{\text{best},n}^{(0)})$,
 $\mathbf{G}_{\text{best}}^{(0)} = \mathbf{x}_k^{(0)}$, $\Gamma_{\text{best}}^{(0)} = \Gamma_{\text{best},k}^{(0)}$, $T = -\Gamma_{\text{best}}^{(0)} / \log(0.2)$,
 $\kappa = \kappa_1 + \kappa_2$, $\chi = \frac{2}{|2 - \kappa + \sqrt{\kappa^2 - 4\kappa}|}$.
- 2 **for** $t = 1$ **to** \mathcal{I}_{\max} **do**
- 3 **if** $\Gamma_{\text{best}} < \varepsilon$ **then break;**
- 4 $\forall n \in \{1, \dots, N\} : p_n^{(t-1)} = \exp(-\frac{(\Gamma_{\text{best},n}^{(t-1)} - \Gamma_{\text{best}}^{(t-1)})}{T})$.
- 5 $p_{\text{sum}} = \sum_{n=1}^N p_n^{(t-1)}$, $p_{\text{bet}} = \text{rand}(0, 1)$.
- 6 $\forall n \in \{1, \dots, N\} : p_n^{(t-1)} = \frac{p_n^{(t-1)}}{p_{\text{sum}}}$.
- 7 **for** $k = 1$ **to** N **do**
- 8 $Q_k = \sum_{n=1}^k p_n^{(t-1)}$.
- 9 **if** $p_{\text{bet}} \leq Q_k$ **then**
- 10 $\mathbf{G}_{\text{rand}}^{(t-1)} = \mathbf{x}_k^{(t-1)}$.
- 11 **break.**
- 12 **end**
- 13 **end**
- 14 **for** $n = 1$ **to** N **do**
- 15 $r_1 = \text{rand}(0, 1)$, $r_2 = \text{rand}(0, 1)$.
- 16 $\mathbf{v}_n^{(t)} = \chi[\mathbf{v}_n^{(t-1)} + \kappa_1 r_1 (\mathbf{P}_{\text{best},n}^{(t-1)} - \mathbf{x}_n^{(t-1)})$
 $\quad + \kappa_2 r_2 (\mathbf{G}_{\text{rand}}^{(t-1)} - \mathbf{x}_n^{(t-1)})]$.
- 17 $\mathbf{x}_n^{(t)} = \mathbf{x}_n^{(t-1)} + \mathbf{v}_n^{(t)}$.
- 18 **if** $\mathbf{x}_n^{(t)} \notin \mathcal{C}$ **then**
- 19 $\Gamma_n^{(t)} = 1000$.
- 20 **end**
- 21 **else**
- 22 $\Gamma_n^{(t)} = \psi(\hat{\mathcal{F}}(f, \mathbf{x}_n^{(t)}), \hat{\Gamma}_L)$.
- 23 **end**
- 24 Updated: $\mathbf{P}_{\text{best},n}^{(t)}$, $\Gamma_{\text{best},n}^{(t)}$, $\mathbf{G}_{\text{best}}^{(t)}$ and $\Gamma_{\text{best}}^{(t)}$.
- 25 **end**
- 26 $T = T \cdot \lambda$.
- 27 **end**
- 28 **return** $\mathbf{C}^* = (C_p^*, C_s^*) = \mathbf{G}_{\text{best}}^{(t)}$.

within its lower and upper limits, where the projection is defined as $\text{Proj}_{\mathcal{C}}(\boldsymbol{\theta}^{(t)}) = \arg \min_{\boldsymbol{\theta} \in \mathcal{C}} \|\boldsymbol{\theta} - \boldsymbol{\theta}^{(t)}\|_2$.

- **Acceptance criteria and termination:** At each iteration, if the predicted input reflection coefficient $\Gamma_{\text{in}}^{(t)}$ at $\boldsymbol{\theta}^{(t)}$ is lower than the threshold ε , the optimization terminates and outputs the optimal configuration (C_p^*, C_s^*) . Otherwise, it proceeds until the maximum iteration number \mathcal{I}_{\max} is reached.

Compared with SAPSO, AD-Adam requires only a single RECBM-Net inference per iteration, thereby significantly re-

Algorithm 2: AD-Adam Impedance Matching

Input: Initial solution $\boldsymbol{\theta}_0$, learning rate α , exponential decay rates β_1, β_2 , stability constant ϵ , maximum iterations \mathcal{I}_{\max} , load reflection coefficient $\hat{\Gamma}_L$, frequency f , threshold ε , tuning range $\mathcal{C} = [C_{p,\min}, C_{p,\max}] \times [C_{s,\min}, C_{s,\max}]$.

Output: Optimal matching solution $\mathbf{C}^* = (C_p^*, C_s^*)$.

- 1 **Initialization:** $t = 0$, $\boldsymbol{\theta}^{(0)} = \boldsymbol{\theta}_0$, $\mathbf{m}_0 = 0$, $\mathbf{v}_0 = 0$.
- 2 **for** $t = 1$ **to** \mathcal{I}_{\max} **do**
- 3 Compute the gradient using AD:
 $\mathbf{g}_t = \nabla_{\boldsymbol{\theta}} \psi(\hat{\mathcal{F}}(f, \boldsymbol{\theta}^{(t-1)}), \hat{\Gamma}_L)$.
- 4 Update \mathbf{m}_t : $\mathbf{m}_t = \beta_1 \mathbf{m}_{t-1} + (1 - \beta_1) \mathbf{g}_t$.
- 5 Update \mathbf{v}_t : $\mathbf{v}_t = \beta_2 \mathbf{v}_{t-1} + (1 - \beta_2) (\mathbf{g}_t \odot \mathbf{g}_t)$.
- 6 Compute bias-corrected estimates:
 $\hat{\mathbf{m}}_t = \frac{\mathbf{m}_t}{1 - \beta_1^t}$, $\hat{\mathbf{v}}_t = \frac{\mathbf{v}_t}{1 - \beta_2^t}$.
- 7 Update matching solution:
 $\boldsymbol{\theta}^{(t)} = \boldsymbol{\theta}^{(t-1)} - \alpha \frac{\hat{\mathbf{m}}_t}{\sqrt{\hat{\mathbf{v}}_t} + \epsilon}$.
- 8 Project $\boldsymbol{\theta}^{(t)}$ onto feasible set \mathcal{C} : $\boldsymbol{\theta}^{(t)} = \text{Proj}_{\mathcal{C}}(\boldsymbol{\theta}^{(t)})$.
- 9 Evaluate reflection coefficient:
 $\Gamma_{\text{in}}^{(t)} = \psi(\hat{\mathcal{F}}(f, \boldsymbol{\theta}^{(t)}), \hat{\Gamma}_L)$.
- 10 **if** $\Gamma_{\text{in}}^{(t)} < \varepsilon$ **then**
- 11 **break.**
- 12 **end**
- 13 **end**
- 14 **return** $\mathbf{C}^* = (C_p^*, C_s^*) = \boldsymbol{\theta}^{(t)}$.

ducing online computational overhead. But its performance may degrade on highly nonconvex objectives, making it more susceptible to local minima and less accurate than SAPSO. Algorithm 2 provides the detailed procedure for impedance matching using AD-Adam.

Proposed strategy (IMS-Net): The two numerical optimization methods discussed above necessitate repeated invocations of RECBM-Net for S-parameters inference, which incurs significant computational overhead. To reduce this burden, we propose a novel strategy that trains an IMS-Net to directly predict the matching solution without iterative DNN evaluation.

Given a predicted $\hat{\Gamma}_L$ and f in the current mismatch scenario, the optimal impedance matching solution (C_p^*, C_s^*) satisfies the implicit equation $\psi(\hat{\mathcal{F}}(f, C_p^*, C_s^*), \hat{\Gamma}_L) = 0$, assuming a perfect match. This solution can be obtained in two steps. First, the predicted $\hat{\mathbf{S}}$ that satisfies the matching condition is computed via the inverse mapping ψ^{-1} . In other words, we solve the equation

$$\frac{\hat{S}_{12} \cdot \hat{S}_{21} \cdot \hat{\Gamma}_L}{1 - \hat{\Gamma}_L \cdot \hat{S}_{22}} + \hat{S}_{11} = 0. \quad (16)$$

Subsequently, the inverse mapping $\hat{\mathcal{F}}^{-1}$ is applied to retrieve the circuit configuration corresponding to the obtained scattering property $\hat{\mathbf{S}}$. Accordingly, the matching solution can be expressed as

$$(C_p^*, C_s^*) = \mathcal{G}(f, \hat{\Gamma}_L), \quad (17)$$

where the composite mapping is defined as $\mathcal{G} = \hat{\mathcal{F}}^{-1} \circ \psi^{-1}$.

Ideally, accurate modeling the composite mapping \mathcal{G} would enable the direct computation of the matching solution. It should be noted that the predicted $\hat{\mathbf{S}}$ from RECBM-Net may not strictly satisfy typical TMN constraints such as passivity ($\mathbf{I} - \hat{\mathbf{S}}^\dagger \hat{\mathbf{S}} \succeq 0$) or reciprocity ($\hat{S}_{12} = \hat{S}_{21}$). Consequently, relying solely on Eq. (16) to determine $\hat{\mathbf{S}}$ results in an underdetermined system with infinitely many solutions, meaning that the mapping ψ^{-1} is multi-valued. Moreover, the circuit behavior \mathcal{F} learned by RECBM-Net does not guarantee that its inverse \mathcal{F}^{-1} is single-valued mapping. Above all, the composite mapping \mathcal{G} may also be multi-valued mapping.

To address the challenges posed by the inherent multi-valued nature of \mathcal{G} and the absence of its analytical expression, we first construct a dataset that enforces a single-valued mapping, and then train an IMS-Net to accurately approximate \mathcal{G} . The main process for obtaining matching solutions using IMS-Net is summarized as follows.

- *Dataset preparation:* Within the TMN's operating frequency band and tunable range, an exhaustive grid is constructed by traversing all possible combinations of frequencies and TMN configurations at a predetermined granularity. Each sample is denoted as $\mathbf{x}^{(i)} = \{f^{(i)}, C_p^{(i)}, C_s^{(i)}\}_{i=1}^{N_d}$, where N_d is the total number of samples. Subsequently, the corresponding $\hat{\mathbf{S}}^{(i)}$ for each configuration $\mathbf{x}^{(i)}$ is predicted using the trained RECBM-Net. Assuming perfect input matching, each predicted $\hat{\mathbf{S}}^{(i)}$ and $\Gamma_{\text{in}} = 0$ are substituted into Eq. (12) to compute the corresponding load reflection coefficient $\hat{\Gamma}_L^{(i)}$. A supervised learning dataset is then constructed as $\{f^{(i)}, \Re(\hat{\Gamma}_L^{(i)}), \Im(\hat{\Gamma}_L^{(i)}), C_p^{(i)}, C_s^{(i)}\}_{i=1}^{N_d}$, where the first three dimensions serve as input features and the last two as outputs labels. This approach not only calculates a large number of load impedances that can be matched by the practical TMN as predicted by RECBM-Net, but also directly provides the corresponding perfect matching solutions without solving the mathematical optimization problem in Eq. (15). Moreover, it guarantees a single-valued mapping from $(f, \hat{\Gamma}_L)$ to the matching solution.
- *Offline training:* IMS-Net employs the same architecture as RECBM-Net, with the only difference being the input and output dimensions (with 3 neurons for input and 2 for output). The dataset is partitioned into training and validation sets. IMS-Net is trained on the former to learn the mapping \mathcal{G} , and its generalization performance is evaluated on the latter.
- *Online inference:* In the deployment phase, the trained IMS-Net takes the predicted load reflection coefficient and operating frequency as input, and directly outputs the corresponding optimal matching solution.

Compared with the two numerical methods discussed above, the integration of IMS-Net with RECBM-Net completely eliminates repeated RECBM-Net evaluations, thereby minimizing online computational overhead. The matching process requires only two inferences: one from RECBM-Net, to predict the the current TMN S-parameters and compute $\hat{\Gamma}_L$, and another from IMS-Net to directly infer the matching solution. More-

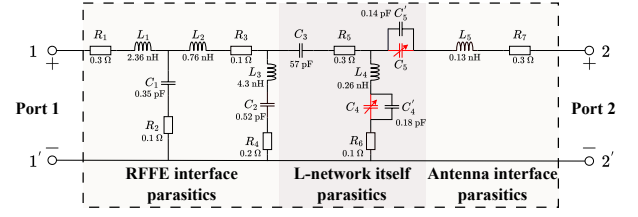


Fig. 6. Schematic of the L-network where 17 parasitic elements are added across the RFFE interface, the L-network itself, and the antenna interface to emulate realistic circuit behavior in practical TMNs.

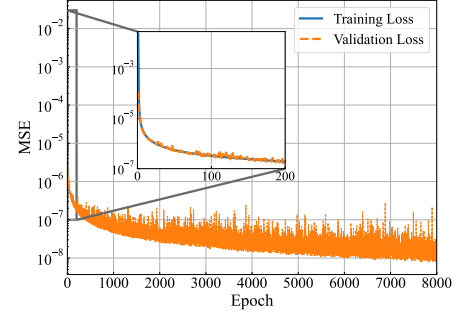


Fig. 7. Training and validation loss (MSE) over epochs.

over, subsequent simulation results demonstrate that IMS-Net achieves exceptionally high accuracy. It is worth noting that IMS-Net functions as a dedicated inverse solver that is tightly coupled with its corresponding RECBM-Net. Therefore, any modification to the RECBM-Net parameters (e.g., learning different TMN circuit behaviors) necessitates retraining the associated IMS-Net.

V. NUMERICAL RESULTS AND DISCUSSION

In this section, we will first utilize RECBM-Net to characterize the circuit behavior of a practical L-network and evaluate its fitting accuracy in detail. Then, we will simulate extensive mismatch scenarios to verify the performance of the proposed data-driven adaptive impedance matching method.

A. Accuracy of RECBM-Net in Modeling Circuit Behavior

To realistically simulate the parasitic effects in practical TMN, we add numerous additional inductors, capacitors, and resistors to the ideal L-network. Fig. 6 illustrates the simulation of an L-network featuring 17 parasitic elements, with the Advanced Design System (ADS) tool employed to collect the S-parameters of the entire two-port network. We systematically sweep through all combinations of operating frequency f and the values of tunable capacitors C_4 and C_5 . Specifically, f is varied from 1.5 GHz to 2 GHz in increments of 0.02 GHz, while C_4 and C_5 are adjusted from 0 to 10 pF in 0.02 pF steps. This comprehensive parameter sweep enabled the construction of an S-parameters dataset that accurately characterizes the practical TMN behavior, comprising a total of 6,500,000 samples.

The dataset is divided into a training set (80%) and a validation set (20%). The training set is used to optimize the model parameters, while the validation set serves to

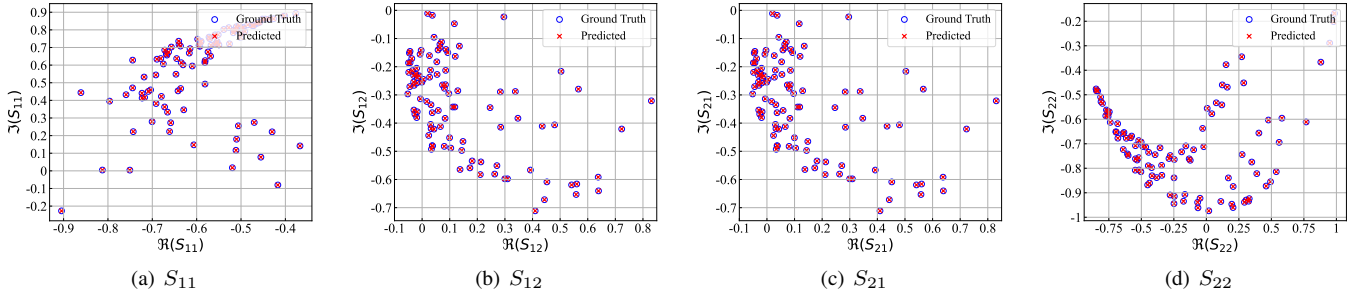


Fig. 8. Comparison between predicted and ground truth S-parameters using RECBM-Net. A total of 100 samples are randomly selected from the test set containing 100,000 samples. The blue circles denote the ground truth, while the red crosses indicate the predicted values.

TABLE I
MEAN PREDICTION ERROR OF S-PARAMETERS USING RECBM-NET.

S-Parameters	Mean Absolute Error		Mean Relative Error	
	Real	Imag	Real	Imag
S_{11}	7.2×10^{-5}	1.0×10^{-4}	0.012%	0.084%
S_{12}	5.3×10^{-5}	5.6×10^{-5}	0.32%	0.039%
S_{21}	5.3×10^{-5}	5.6×10^{-5}	0.319%	0.038%
S_{22}	9.2×10^{-5}	7.6×10^{-5}	0.163%	0.012%

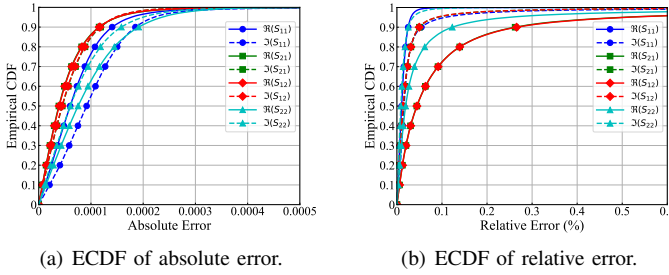


Fig. 9. Empirical cumulative distribution function (ECDF) of the absolute and relative errors of RECBM-Net predictions for each real and imaginary component of the S-parameters on the test set.

evaluate the model's generalization performance. Given the scale disparities between the frequency feature and the tunable capacitors, we apply min-max normalization to all input features to ensure training stability. In terms of the loss function, we employ the mean squared error (MSE) to quantify the discrepancy between the model's prediction and the actual values. It is defined as

$$L(\theta) = \frac{1}{8N} \sum_{i=1}^N \|\mathbf{y}_i - \hat{\mathbf{y}}_i\|_2^2, \quad (18)$$

where $L(\theta)$ is the loss function used to measure the average difference between the predicted vectors $\hat{\mathbf{y}}_i \in \mathbb{R}^8$ and the ground truth vectors $\mathbf{y}_i \in \mathbb{R}^8$ across all N training samples. The Adam optimizer is selected to train the RECBM-Net with the initial learning rate set to 5×10^{-8} . A batch size of 512 is utilized, and the model is trained for 8000 epochs.

The model was trained using four NVIDIA GeForce RTX 2080 Ti GPUs with the PyTorch framework. As shown in Fig. 7, the loss on the training set converges to 1.5×10^{-8} , while the validation set loss stabilizes at 9.1×10^{-9} . The

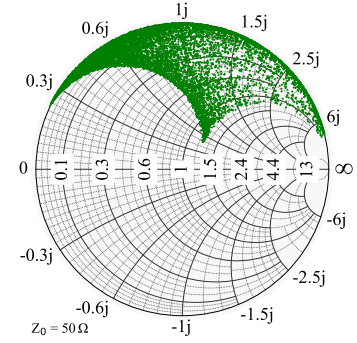


Fig. 10. Distribution of mismatched impedances under 9000 simulated mismatch scenarios over the frequency range from 1.5 GHz to 2 GHz.

extremely low validation loss provides initial evidence of the model's generalization ability. To further evaluate the RECBM-Net's ability to predict S-parameters, we constructed a test set of 100,000 samples, enabling a more comprehensive assessment of the model's performance on unseen data. For each test sample, the frequency is uniformly sampled between 1.5 and 2 GHz, and the capacitor values for C_4 and C_5 are uniformly sampled between 0 and 10 pF. Fig. 8 presents a scatter plot comparing the predicted values and the ground truth S-parameters for 100 randomly selected samples from the test set. It can be observed that RECBM-Net achieves accurate prediction of the S-parameters. In addition, Table I illustrates that the mean absolute error of the S-parameters predictions in each dimension on the entire test set is on the order of 10^{-5} , while the corresponding mean relative error is on the order of 10^{-4} (i.e., far below 1%). More specifically, as depicted in Fig. 9, the error distribution computed over the entire test set reveals that in over 95% of the samples, the absolute error in each dimension of the predicted S-parameters is below 3×10^{-4} , while the relative error is below 0.6%. These mean error and statistical error distribution results on the extensive test set collectively demonstrate that the model can predict the circuit behavior of a practical L-network with exceptional precision, thereby supporting the subsequent accurate determination of matching solution.

B. Performance of Data-Driven Impedance Matching Method

We simulate real-world mismatch conditions to verify the proposed purely data-driven impedance matching method and

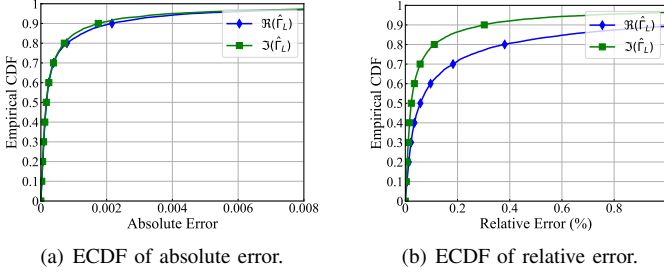


Fig. 11. ECDF of the absolute and relative errors between the true load reflection coefficient and one computed by applying Eq. (12) to the S-parameters predicted by RECBM-Net. The statistics are computed over 9000 simulated mismatch scenarios.

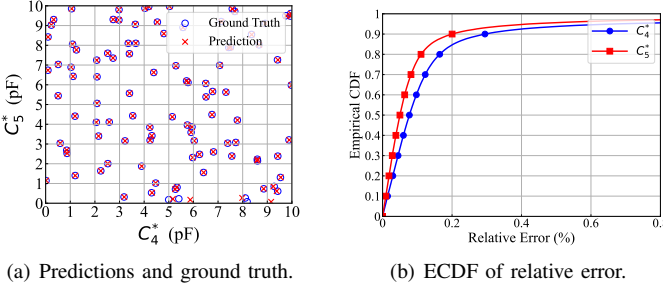


Fig. 12. Comparison on the test set between the matching solution predicted by IMS-Net and the perfect matching solution derived from RECBM-Net.

compare the performance of three matching solution determination strategies. We randomly generated 9000 combinations of f , C_4^* and C_5^* within the tunable range. Assuming the input is perfectly matched (i.e., $\Gamma_{in} = 0$), the mismatched load reflection coefficient Γ_L is derived based on the practical L-network topology depicted in Fig. 6. This yields 9000 sets of load impedance and corresponding TMN configurations (C_4^*, C_5^*) that achieve perfect impedance matching. To simulate the mismatch, new values $(C_4^{\text{now}}, C_5^{\text{now}})$ for tunable capacitors are generated within the tunable range and corresponding Γ_{in} is calculated based on the practical L-network circuit model. Finally, we generated a mismatched dataset that simulates real-world impedance mismatch. Each sample comprises the operating frequency f , the TMN circuit configuration $(C_4^{\text{now}}, C_5^{\text{now}})$, the measured input port reflection coefficient Γ_{in} , and the actual load reflection coefficient Γ_L corresponding to the current mismatch scenario. Since testing the adaptive impedance matching methods within the matching forbidden region is meaningless, this simulation method ensures that the mismatched impedance Γ_L remains outside matching forbidden region.

As shown in Fig. 10, the simulated mismatched load impedance deviates significantly from 50Ω . Following the impedance matching process described in Section IV-B, we first use RECBM-Net to infer the S-parameters corresponding to $(f, C_4^{\text{now}}, C_5^{\text{now}})$ and calculate the predicted load reflection coefficient $\hat{\Gamma}_L$. Fig. 11 illustrates the empirical cumulative distribution functions (ECDFs) of the absolute and relative errors between the predicted $\hat{\Gamma}_L$ and the actual Γ_L for all mismatched samples in the dataset. Over 95% of the samples

TABLE II
HYPERPARAMETER SETTINGS FOR THE MATCHING STRATEGIES SAPSO AND AD-ADAM

Parameter	SAPSO	AD-Adam
Number of particles N	50	—
Individual learning factor κ_1	2.05	—
Social learning factor κ_2	2.05	—
Cooling factor λ	0.5	—
Initial solution θ_0	—	(5 pF, 5 pF)
Learning rate α	—	0.05
Exponential decay rates β_1, β_2	—	0.9, 0.999
Stability constant ϵ	—	10^{-8}
Maximum iterations \mathcal{I}_{\max}	100	500
Early stopping threshold ε	0.005	0.005

exhibit absolute errors below 0.006 for both the real and imaginary parts of $\hat{\Gamma}_L$, while over 90% show the relative errors under 1% in both parts. In summary, the load impedance estimated via the RECBM-Net surrogate model exhibits excellent consistency with the actual impedance, thereby enabling the matching solution determination strategies to effectively minimize the actual input reflection coefficient.

Utilizing the dataset generation method described in Sec. IV-B, we constructed the training dataset for IMS-Net. The traversal granularity for combinations of the operating frequency and TMN configurations is identical to that employed in the RECBM-Net training dataset (Sec. V-A). Similarly, we generated a supervised learning dataset formatted as $\{f, \Re(\hat{\Gamma}_L), \Im(\hat{\Gamma}_L), C_4^*, C_5^*\}$ containing 6,500,000 samples with the MSE serving as the loss function. To amplify the gradient signal during backpropagation, the dataset labels were scaled by a factor of 10. Subsequently, the dataset was partitioned into 80% for training and 20% for validation. IMS-Net was then trained on the same hardware platform using the Adam optimizer with an initial learning rate of 0.00002. Training was conducted for 3000 epochs with a batch size of 512, ultimately converging to training and validation losses of 0.052 and 0.051, respectively. To further validate IMS-Net's ability to predict matching solutions on unseen data, we generated a test set comprising 100,000 combinations by randomly sampling both the operating frequency and TMN configuration within a tunable range. Fig. 12 illustrates that IMS-Net reliably predicts matching solutions on the test set, with nearly 95% of samples achieving a relative error below 0.6%. Notably, when C_5^* is extremely close to 0, the prediction accuracy exhibits a minor decline, while the overall performance remains robust.

Finally, we evaluate the matching performance of the three matching solution determination strategies on the same 9,000 mismatch samples generate earlier, each reflecting a realistic mismatch scenario. Table II summarizes the hyperparameter settings for the two numerical optimization strategies. Fig. 13 illustrates that when the load reflection coefficient is derived based on the ideal L-network topology and the matching solution is calculated using the closed-form expressions in Eq. (5), the resulting solution even degrades matching performance. In contrast, the purely data-driven impedance matching method based on SAPSO achieves a reflection coefficient below 0.2 for 96.01% of the mismatched samples, slightly outperforming

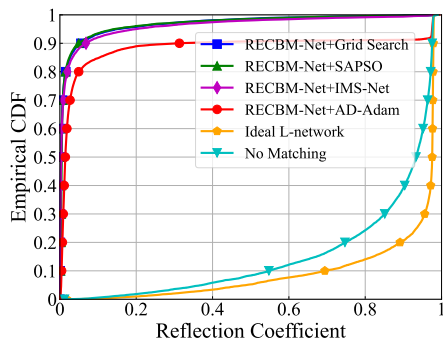


Fig. 13. Comparison of the matching performance of solutions obtained by the proposed data-driven approach with different determination strategies, those analytically derived from the ideal L-network circuit model.

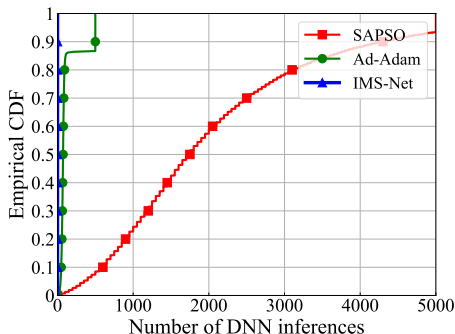


Fig. 14. ECDF of the number of DNN inferences required by three matching solution determination strategies (SAPSO, AD-Adam, and IMS-Net) across 9,000 simulated mismatch scenarios.

the exhaustive grid search with a granularity of $0.01 \text{ pF} \times 0.01 \text{ pF}$, which achieves the same target for 95.76% of the samples. A reflection coefficient below 0.2 is generally considered to indicate a high-quality impedance match in practical engineering applications [44], corresponding to approximately 96% of the incident power being delivered to the antenna. IMS-Net also demonstrates high matching accuracy, reducing the reflection coefficient below 0.2 for 95% of the samples. In comparison, the AD-Adam method yields lower matching accuracy, with 88.95% of the samples satisfying the same reflection coefficient threshold. This suboptimal performance can be attributed to the inherent limitations of gradient-based optimization algorithms when applied to non-convex objective landscapes.

Fig. 14 presents the online computational overhead of the three matching solution computation strategies, evaluated over 9,000 simulated mismatch scenarios. The overhead is quantified by the number of DNN inferences required, and their distributions are compared using ECDFs. SAPSO achieves the highest matching accuracy among the three strategies, but incurs the highest computational overhead. It requires thousands of RECBM-Net inferences per sample due to its population-based search process. In contrast, AD-Adam typically requires dozens of DNN inferences. Furthermore, IMS-Net computes the matching solution using only a single DNN inference, making it highly efficient for real-time applications. Although AD-Adam yields lower matching accuracy, it offers a substantial advantage in computational efficiency

compared to SAPSO. IMS-Net achieves both high matching accuracy and minimal online computational overhead but it requires an offline training phase, which introduces additional computational overhead prior to deployment. In summary, the proposed purely data-driven adaptive impedance matching method does not rely on explicit circuit topology and remain effective and accurate when the practical circuit topology deviates significantly from the ideal TMN.

VI. CONCLUSION

In this work, we have proposed a purely data-driven adaptive impedance matching method that is robust to parasitic effects. First, we have designed RECBM-Net, a DNN that maps the operating state of a practical L-network to its corresponding S-parameters. Then, we have formulated the impedance matching task via the trained surrogate model as a mathematical optimization problem, and introduced two numerical optimization strategies with different online computational overhead. Finally, to avoid repeated RECBM-Net inference during matching, we have proposed IMS-Net that directly predicts the optimal solution in a single forward pass. Simulation results have shown that RECBM-Net achieves exceptionally high prediction accuracy of the S-parameters, with the absolute error for each component being on the order of 10^{-4} . In the simulated mismatched scenarios, SAPSO has achieved higher matching accuracy than AD-Adam, with the trade-off of substantially increased computational overhead. IMS-Net has significantly reduced the online inference overhead while maintaining excellent performance, lowering the reflection coefficient below 0.2 for 95% of samples.

REFERENCES

- [1] E. Zenteno, M. Isaksson, and P. Händel, "Output impedance mismatch effects on the linearity performance of digitally predistorted power amplifiers," *IEEE Trans. Microw. Theory Techn.*, vol. 63, no. 2, pp. 754–765, Feb. 2015.
- [2] A. Van Bezooijen, F. van Straten, R. Mahmoudi, and A. H. M. van Roermund, "Power amplifier protection by adaptive output power control," *IEEE J. Solid-State Circuits*, vol. 42, no. 9, pp. 1834–1841, Sep. 2007.
- [3] M. Alibakhshikenari, B. S. Virdee, C. H. See, R. A. Abd-Alhameed, F. Falcone, and E. Limiti, "Automated reconfigurable antenna impedance for optimum power transfer," in *Proc. IEEE Asia-Pac. Microw. Conf. (APMC)*, Dec. 2019, pp. 1461–1463.
- [4] K. R. Boyle, "The performance of GSM 900 antennas in the presence of people and phantoms," in *Proc. 12th Int. Conf. Antennas Propag. (ICAP)*, Mar. 2003, pp. 35–38.
- [5] K. Ogawa and T. Matsuyoshi, "An analysis of the performance of a handset diversity antenna influenced by head, hand, and shoulder effects at 900 MHz. I. Effective gain characteristics," *IEEE Trans. Veh. Technol.*, vol. 50, no. 3, pp. 830–844, May. 2001.
- [6] K. R. Boyle, Y. Yuan, and L. P. Ligthart, "Analysis of mobile phone antenna impedance variations with user proximity," *IEEE Trans. Antennas Propag.*, vol. 55, no. 2, pp. 364–372, Feb. 2007.
- [7] J. W. Adams, L. Chen, P. Serano, A. Nazarian, R. Ludwig, and S. N. Makarov, "Miniaturized dual antiphasic patch antenna radiating into the human body at 2.4 GHz," *IEEE J. Electromagn. RF Microw. Med. Biol.*, vol. 7, no. 2, pp. 182–186, Jun. 2023.
- [8] G. Sacco, D. Nikolayev, R. Sauleau, and M. Zhadobov, "Antenna/human body coupling in 5G millimeter-wave bands: Do age and clothing matter?" *IEEE J. Microw.*, vol. 1, no. 2, pp. 593–600, Apr. 2021.
- [9] F. Kong, M. Ghovanloo, and G. D. Durgin, "An adaptive impedance matching transmitter for a wireless intraoral tongue-controlled assistive technology," *IEEE Trans. Circuits Syst. II, Exp. Briefs*, vol. 67, no. 2, pp. 240–244, Feb. 2020.

- [10] A. Van Bezooijen *et al.*, "RF-MEMS based adaptive antenna matching module," in *Proc. IEEE Radio Freq. Integr. Circuits (RFIC) Symp.*, Jun. 2007, pp. 573–576.
- [11] I. Ida, J. Takada, T. Toda, and Y. Oishi, "An adaptive impedance matching system for mobile communication antennas," in *Proc. IEEE Antennas Propag. Soc. AP. S. Int. Symp.*, Jun. 2004, pp. 3203–3206.
- [12] J. D. Mingo, A. Valdovinos, A. Crespo, D. Navarro, and P. Garcia, "An RF electronically controlled impedance tuning network design and its application to an antenna input impedance automatic matching system," *IEEE Trans. Microw. Theory Techn.*, vol. 52, no. 2, pp. 489–497, Feb. 2004.
- [13] Y. Sun and W. K. Lau, "Antenna impedance matching using genetic algorithms," in *Proc. IEE Nat. Conf. Antennas Propag.*, Apr. 1999, pp. 31–36.
- [14] N. J. Smith, C.-C. Chen, and J. L. Volakis, "An improved topology for adaptive agile impedance tuners," *IEEE Antennas Wireless Propag. Lett.*, vol. 12, pp. 92–95, 2013.
- [15] Y. Ma and G. Wu, "Automatic impedance matching using simulated annealing particle swarm optimization algorithms for RF circuit," in *Proc. IEEE Adv. Inf. Technol. Electron. Autom. Control Conf. (IAEAC)*, Dec. 2015, pp. 581–584.
- [16] K. Ogawa, T. Takahashi, Y. Koyanagi, and K. Ito, "Automatic impedance matching of an active helical antenna near a human operator," in *Proc. 33rd Eur. Microwave Conf.*, 2003, pp. 1271–1274.
- [17] B. Xiong, L. Yang, and T. Cao, "A novel tuning method for impedance matching network based on linear fractional transformation," *IEEE Trans. Circuits Syst. II, Exp. Briefs*, vol. 67, no. 6, pp. 1039–1043, Jun. 2020.
- [18] P. Sjöblom and H. Sjöland, "An adaptive impedance tuning CMOS circuit for ISM 2.4-GHz band," *IEEE Trans. Circuits Syst. I, Reg. Papers*, vol. 52, no. 6, pp. 1115–1124, Jun. 2005.
- [19] S. M. Ali, M. Buckley, J. Deforge, J. Warden, and A. Danak, "Dynamic measurement of complex impedance in real-time for smart handset applications," *IEEE Trans. Microw. Theory Techn.*, vol. 61, no. 9, pp. 3453–3460, Sep. 2013.
- [20] M. Thompson and J. K. Fidler, "Determination of the impedance matching domain of impedance matching networks," *IEEE Trans. Circuits Syst. I, Reg. Papers*, vol. 51, no. 10, pp. 2098–2106, Oct. 2004.
- [21] A. Van Bezooijen, M. A. De Jongh, F. Van Straten, R. Mahmoudi, and A. H. Van Roermund, "Adaptive impedance-matching techniques for controlling 1 networks," *IEEE Trans. Circuits Syst. I, Reg. Papers*, vol. 57, no. 2, pp. 495–505, Feb. 2009.
- [22] Q. Gu, J. R. De Luis, A. S. Morris, and J. Hilbert, "An analytical algorithm for Pi-network impedance tuners," *IEEE Trans. Circuits Syst. I, Reg. Papers*, vol. 58, no. 12, pp. 2894–2905, Dec. 2011.
- [23] Q. Gu and A. S. Morris, "A new method for matching network adaptive control," *IEEE Trans. Microw. Theory Techn.*, vol. 61, no. 1, pp. 587–595, Jan. 2012.
- [24] J. H. Kim and J. Bang, "Antenna impedance matching using deep learning," *Sensors*, vol. 21, no. 20, p. 6766, Oct. 2021.
- [25] M. M. Hasan and M. Cheffena, "Adaptive antenna impedance matching using low-complexity shallow learning model," *IEEE Access*, vol. 11, pp. 74 101–74 111, 2023.
- [26] S. Jeong, T.-H. Lin, and M. M. Tentzeris, "A real-time range-adaptive impedance matching utilizing a machine learning strategy based on neural networks for wireless power transfer systems," *IEEE Trans. Microw. Theory Techn.*, vol. 67, no. 12, pp. 5340–5347, Dec. 2019.
- [27] W. Cheng, L. Chen, and W. Wang, "A time-frequency domain adaptive impedance matching approach based on deep neural network," *IEEE Antennas Wireless Propag. Lett.*, vol. 24, no. 1, pp. 202–206, Jan. 2025.
- [28] X. Zhao, T. Nguyen, R. Burgos, and D. Dong, "Novel current sensor based on parasitic inductance with adaptive compensation for parasitic resistance," *IEEE Trans. Power Electron.*, vol. 40, no. 5, pp. 6403–6412, May. 2025.
- [29] Z. Fang *et al.*, "Closed-form expressions of parasitic parameters for different sidewall roughness of through-silicon vias interconnects," *IEEE Trans. Electron Devices*, vol. 71, no. 2, pp. 1160–1165, Feb. 2024.
- [30] Y. Xiao, Z. Zhou, H. Wang, and J. Ren, "Simulation research on parasitic parameter extraction of LDO power chip package based on ANSYS Q3D," in *Proc. 7th Int. Conf. Autom., Control Robots (ICACR)*, Aug. 2023, pp. 92–96.
- [31] K. Song, J. Gao, G. T. Flowers, Z. Wang, W. Yi, and Z. Cheng, "Modeling and analysis of signal integrity of ball grid array packages with failed ground solder balls," *IEEE Trans. Compon., Packag., Manuf. Techn.*, vol. 12, no. 2, pp. 306–315, Feb. 2022.
- [32] A. Afsari, B. Van Veen, and N. Behdad, "An electronically reconfigurable matching and decoupling network for two-element HF antenna arrays," *IEEE Trans. Antennas Propag.*, vol. 72, no. 8, pp. 6332–6347, Aug. 2024.
- [33] E. L. Firrao, A.-J. Annema, and B. Nauta, "An automatic antenna tuning system using only RF signal amplitudes," *IEEE Trans. Circuits Syst. II: Exp. Briefs*, vol. 55, no. 9, pp. 833–837, Sep. 2008.
- [34] A. R. Suvarna, V. Bhagavatula, and J. C. Rudell, "Transformer-based tunable matching network design techniques in 40-nm CMOS," *IEEE Trans. Circuits Syst. II, Exp. Briefs*, vol. 63, no. 7, pp. 658–662, Jul. 2016.
- [35] W. C. E. Neo *et al.*, "Adaptive multi-band multi-mode power amplifier using integrated varactor-based tunable matching networks," *IEEE J. Solid-State Circuits*, vol. 41, no. 9, pp. 2166–2176, Sep. 2006.
- [36] Q. Shen and N. S. Barker, "Distributed MEMS tunable matching network using minimal-contact RF-MEMS varactors," *IEEE Trans. Microw. Theory Technol.*, vol. 54, no. 6, pp. 2646–2658, Jun. 2006.
- [37] T. Vaha-Heikkilä, J. Varis, J. Tuovinen, and G. M. Rebeiz, "A 20–50 GHz RF MEMS single-stub impedance tuner," *IEEE Microw. Wireless Compon. Lett.*, vol. 15, no. 4, pp. 205–207, Apr. 2005.
- [38] P. Sjöblom and H. Sjöland, "Measured CMOS switched high-quality capacitors in a reconfigurable matching network," *IEEE Trans. Circuits Syst. II, Exp. Briefs*, vol. 54, no. 10, pp. 858–862, Oct. 2007.
- [39] T. Wang, T. Michalka, and G. R. Luevano, "Accurate and efficient impedance matching method in the presence of on-board and SMT parasitic components," in *Proc. IEEE Conf. Electrical Perform. Electronic Packaging and Syst. (EPEPS)*, Oct. 2017, pp. 1–3.
- [40] M. T. Ivrlac and J. A. Nossek, "Toward a circuit theory of communication," *IEEE Trans. Circuits Syst. I, Reg. Papers*, vol. 57, no. 7, pp. 1663–1683, Jul. 2010.
- [41] K. Hornik, M. Stinchcombe, and H. White, "Multilayer feedforward networks are universal approximators," *Neural Netw.*, vol. 2, no. 5, pp. 359–366, 1989.
- [42] D. P. Kingma and J. Ba, "Adam: A method for stochastic optimization," *arXiv:1412.6980*, 2014.
- [43] M. Bartholomew-Biggs, S. Brown, B. Christianson, and L. Dixon, "Automatic differentiation of algorithms," *J. Comput. Appl. Math.*, vol. 124, no. 1–2, pp. 171–190, 2000.
- [44] A. Kuchikulla, "Applying impedance tuning to maximize antenna performance in 5G phones," *Qorvo, Greensboro, NC, USA, Tech. Rep.*, 2020.